Enhancement of VUV and EUV generation by field-controlled resonance structures of diatomic molecules

John Heslar,[1] Dmitry A. Telnov,[2,*] and Shih-I Chu[1,3,†]

[1]*Center for Quantum Science and Engineering, and Center for Advanced Study in Theoretical Sciences, Department of Physics, National Taiwan University, Taipei 10617, Taiwan*

[2]*Department of Physics, St. Petersburg State University, 7-9 Universitetskaya nab., St. Petersburg 199034, Russia*

[3]*Department of Chemistry, University of Kansas, Lawrence, Kansas 66045, USA*

(Received 2 February 2016; revised manuscript received 29 March 2016; published 1 June 2016)

Below- and near-threshold harmonic generation provides a potential approach to achieve a high conversion efficiency of vacuum-ultraviolet and extreme-ultraviolet sources for the advancement of spectroscopy. Here, we perform a time-dependent density functional theory study for the nonperturbative treatment of below- and near-threshold harmonic generation of CO and N_2 diatomic molecules subject to short near-infrared laser pulses and aligned parallel to the laser field polarization. We find that with the use of different driving laser pulse shapes, we can control and enhance harmonic generation through the excited-state resonance structures. Depending on the pulse shape, the enhancement can reach five to seven orders of magnitude as compared to the reference sine-squared laser pulse of the same duration. The results for different driving laser intensities are also presented and discussed in detail.

DOI: 10.1103/PhysRevA.93.063401

I. INTRODUCTION

High-order harmonic generation (HHG) has been the enabling technology for ultrafast science in the vacuum-ultraviolet (VUV) and extreme-ultraviolet (EUV) spectral regions [1–3]. High conversion efficiency of HHG is a goal that the experimentalists are trying to achieve in order to create sources of intense VUV and EUV radiation [4–13]. Lately, numerous advancements have been made in VUV [4,8,10–12] and XUV [6–8] pulse generation that can be applied to many areas in ultrafast science and technology [5,9,13]. However, achieving efficient VUV or EUV conversion of corresponding weak to moderate driving pulses is challenging and lately major attention has been focused in this area of research [4–7]. Conversion efficiencies for moderate peak power driving lasers that have been achieved are orders of magnitude behind the values that have been demonstrated with loose focusing strong peak power driving pulses [14–23]. Recently, Wang *et al.* [7] demonstrated an enhanced highly efficient source of femtosecond EUV pulses where there enhancements arose from both wavelength scaling of the atomic dipole and improved spatiotemporal phase matching.

The goal to boost the conversion efficiency can be achieved in different ways. One approach is to increase the repetition rates with weaker driving lasers, but here one needs to make the laser focus tight to ensure high enough intensity in the focus for efficient HHG by individual atoms or molecules. However, making the laser focus tight significantly worsens the phase-matching conditions in the macroscopic medium. Another approach to enhance HHG is to increase the intensity of the driving laser pulses. With stronger driving pulses, the laser focus can be made loose, thus improving the phase-matching conditions, but in this case the conversion efficiency suffers from low repetition rates. The third approach to boost the conversion efficiency, which we follow in this paper, is to enhance the HHG signal on the microscopic level, for individual atoms or molecules.

As we have recently demonstrated along with the experimentalists [4], below-threshold harmonics represent one such possibility, where phase matching in the argon medium near atomic resonances enables enhancement of coherent VUV line emissions. Such emissions can be controlled by temporal structures of the few-cycle driving laser field with an intensity of only $\sim 1 \times 10^{13}$ W/cm^2 [4], which is achievable directly from few-cycle femtosecond oscillators with nanojoule energy. In the present contribution, we explore enhancement of VUV and EUV line emissions on the microscopic level by field-controlled resonance structures of homonuclear (N_2) and heteronculcear (CO) diatomic molecules, which in return give narrow linewidth VUV and EUV radiation. In this context, we will be focusing on the below- and near-threshold harmonics. In the past, major attention was focused on the HHG regime above the ionization threshold where the semiclassical three-step model and strong field approximation are effective to explain the process. However, neglecting the electronic structure of the target and interaction between the electron and molecular core results in inadequate description in the below- and near-threshold HHG regime.

In this work, we present an all-electron time-dependent density functional theory (TDDFT) with proper long-range potentials to study the HHG regime of below- and near-threshold harmonics in CO and N_2 molecules. In this contribution, we identify and study excited-state resonance structures in CO and N_2 molecules for different driving laser intensities. Furthermore, we investigate the conversion efficiency and show how to improve it using different types of driving laser pulses and pulse shapes. Our calculations reveal that a five orders of magnitude increase of the VUV line radiation in CO can be enabled on average, and the corresponding enhancement of EUV line emission in N_2 can reach up to seven orders of magnitude. Finally, we compare different types of the laser pulse and pulse shapes (we have tried five

*d.telnov@spbu.ru
†sichu@ku.edu

variants) and make a conclusion which one provides the best enhancement. We believe that the proposed method can be applied to other atomic and molecular systems to dramatically improve the conversion efficiency through the excited-state resonance structures, thus opening the door to the development of compact, high-flux VUV and EUV light sources.

The organization of this paper is as follows. In Sec. II, we briefly describe the *all-electron* TDDFT formalism for the general treatment of the multiphoton dynamics of heteronuclear and homonuclear diatomic molecular systems. In Sec. III, we analyze the below- and near-threshold resonance structures in the radiation spectra of CO and N_2 molecules and study the evolution of these resonance structures with different driving laser intensities. In Sec. IV, we investigate the role of field-controlled enhancement of these resonance structures by applying five different laser pulse shapes and also clearly show the line emissions can be enhanced orders of magnitude. While the VUV or EUV emissions are greatly enhanced orders of magnitude, they still exhibit narrow linewidths. Section IV contains concluding remarks.

II. TIME-DEPENDENT DFT FOR NONPERTURBATIVE TREATMENT OF DIATOMIC MOLECULES IN ONE- AND TWO-COLOR LASER FIELDS

The basic equations of TDDFT are the time-dependent one-electron Kohn-Sham equations [24] for spin orbitals $\psi_{i\sigma}(\boldsymbol{r},t)$ which involve an effective potential $v_{\mathrm{eff},\sigma}(\boldsymbol{r},t)$ (in atomic units):

$$i\frac{\partial}{\partial t}\psi_{i\sigma}(\boldsymbol{r},t)=\left[-\frac{1}{2}\nabla^2+v_{\mathrm{eff},\sigma}(\boldsymbol{r},t)\right]\psi_{i\sigma}(\boldsymbol{r},t),\quad i=1,2,\ldots,N_\sigma \tag{1}$$

where $N_\sigma(=N_\uparrow$ or $N_\downarrow)$ is the total number of electrons for a given spin σ, and the total number of electrons in the system is $N=\sum_\sigma N_\sigma$. The time-dependent effective potential $v_{\mathrm{eff},\sigma}(\boldsymbol{r},t)$ is a functional of the electron spin densities $\rho_\sigma(\boldsymbol{r},t)$ which are related to the spin orbitals as follows:

$$\rho_\sigma(\boldsymbol{r},t)=\sum_{i=1}^{N_\sigma}|\psi_{i\sigma}(\boldsymbol{r},t)|^2 \tag{2}$$

(the summation includes all spin orbitals with the same spin). The effective potential $v_{\mathrm{eff},\sigma}(\boldsymbol{r},t)$ in Eq. (1) can be written in the following general form:

$$v_{\mathrm{eff},\sigma}(\boldsymbol{r},t)=v_{\mathrm{H}}(\boldsymbol{r},t)+v_{\mathrm{ext}}(\boldsymbol{r},t)+v_{\mathrm{xc},\sigma}(\boldsymbol{r},t), \tag{3}$$

where

$$v_{\mathrm{H}}(\boldsymbol{r},t)=\int\frac{\rho(\boldsymbol{r}',t)}{|\boldsymbol{r}-\boldsymbol{r}'|}d\boldsymbol{r}' \tag{4}$$

is the Hartree potential due to electron-electron Coulomb interaction and $\rho(\boldsymbol{r},t)$ is the total electron density

$$\rho(\boldsymbol{r},t)=\sum_\sigma\rho_\sigma(\boldsymbol{r},t). \tag{5}$$

$v_{\mathrm{ext}}(\boldsymbol{r},t)$ is the "external" potential due to the interaction of the electron with the external laser field and the nuclei. In the case of homonuclear or heteronuclear diatomic molecules in a linearly polarized external laser field $[\boldsymbol{E}_1(t)\cdot\boldsymbol{r}]$ or fields $[\boldsymbol{E}_1(t)\cdot\boldsymbol{r}+\boldsymbol{E}_2(t)\cdot\boldsymbol{r}]$, we have

$$v_{\mathrm{ext}}(\boldsymbol{r},t)=-\frac{Z_1}{|\boldsymbol{R}_1-\boldsymbol{r}|}-\frac{Z_2}{|\boldsymbol{R}_2-\boldsymbol{r}|}+[\boldsymbol{E}_1(t)\cdot\boldsymbol{r}+\boldsymbol{E}_2(t)\cdot\boldsymbol{r}], \tag{6}$$

where $\boldsymbol{r}$ is the electronic coordinate, $E_1(t)$ and $E_2(t)$ are the electric field amplitudes where the laser field is polarized along the molecular axis, $\boldsymbol{R}_1$ and $\boldsymbol{R}_2$ are the coordinates of the two nuclei at their fixed equilibrium positions, and Z_1 and Z_2 are the electric charges of the two nuclei, respectively. The internuclear separation R is equal to $|\boldsymbol{R}_2-\boldsymbol{R}_1|$. Finally, $v_{\mathrm{xc},\sigma}(\boldsymbol{r},t)$ is the time-dependent exchange-correlation (xc) potential. Since the exact form of $v_{\mathrm{xc},\sigma}(\boldsymbol{r},t)$ is unknown, the *adiabatic* approximation is often used [25–30]:

$$v_{\mathrm{xc},\sigma}(\boldsymbol{r},t)=v_{\mathrm{xc},\sigma}[\rho_\sigma]|_{\rho_\sigma=\rho_\sigma(\boldsymbol{r},t)}. \tag{7}$$

When these potentials, determined by the time-independent ground-state density functional theory (DFT), are used along with TDDFT in the electronic structure calculations, both inner shell and excited states can be calculated rather accurately [31]. In this work, we utilize the improved van Leeuwen–Baerends LBα xc potential [32]. The LBα contains two empirical parameters α and β and has the following explicit form, in the adiabatic approximation:

$$v_{\mathrm{xc},\sigma}^{\mathrm{LB}\alpha}(\boldsymbol{r},t)=\alpha v_{\mathrm{x},\sigma}^{\mathrm{LSDA}}(\boldsymbol{r},t)+v_{\mathrm{c},\sigma}^{\mathrm{LSDA}}(\boldsymbol{r},t)-\frac{\beta x_\sigma^2(\boldsymbol{r},t)\rho_\sigma^{1/3}(\boldsymbol{r},t)}{1+3\beta x_\sigma(\boldsymbol{r},t)\ln\left\{x_\sigma(\boldsymbol{r},t)+\left[x_\sigma^2(\boldsymbol{r},t)+1\right]^{1/2}\right\}}. \tag{8}$$

Here, ρ_σ is the electron density with spin σ, and we use $\alpha=1.19$ and $\beta=0.01$ [27–30]. The first two terms in Eq. (8), $v_{\mathrm{x},\sigma}^{\mathrm{LSDA}}$ and $v_{\mathrm{c},\sigma}^{\mathrm{LSDA}}$, are the local spin density approximation (LSDA) exchange and correlation potentials that do *not* have the correct Coulombic asymptotic behavior. The last term in Eq. (8) is the nonlocal gradient correction with $x_\sigma(\boldsymbol{r})=|\nabla\rho_\sigma(\boldsymbol{r})|/\rho_\sigma^{4/3}(\boldsymbol{r})$, which ensures the proper long-range Coulombic asymptotic potential $v_{\mathrm{xc},\sigma}^{\mathrm{LB}\alpha}\to-1/r$ as $r\to\infty$. Note that if the conventional xc energy functional forms taken from LSDA or generalized gradient approximation (GGA) [33,34] are used, the corresponding xc potential $v_{\mathrm{xc},\sigma}(\boldsymbol{r},t)$ will not possess the correct long-range asymptotic $(-1/r)$ behavior [35]. For the time-independent case, this exchange-correlation LBα potential has been found to be reliable for atomic and molecular DFT calculations [4,27–30,32,36–38].

For the numerical solution of the TDDFT equations for diatomic molecules with proper long-range potential, we have recently developed a time-dependent generalized pseudospectral (TDGPS) method in prolate spheroidal coordinate system [27–30,38–41]. The advantage of this method is that it allows *nonuniform* and optimal spatial grid discretization (denser mesh near each nucleus and sparser mesh at larger electron-nucleus separations). This improves greatly both the accuracy and the efficiency of the electronic structure and time-dependent calculations with the use of only a modest number

TABLE I. Comparison of the field-free molecular orbital energy levels of CO and N_2, calculated with the LBα potential, and the experimental ionization potentials (in a.u.).

			CO			
Orbital	1σ	2σ	3σ	4σ	1π	5σ
Expt. [44]	19.9367	10.8742	1.3964	0.7239	0.6247	0.5144
LBα	19.7721	10.7723	1.2601	0.7247	0.6276	0.5093
			N_2			
Orbital	$1\sigma_g$	$1\sigma_u$	$2\sigma_g$	$2\sigma_u$	$1\pi_u$	$3\sigma_g$
Expt. [45–47]	15.0492	15.0492	1.3708	0.6883	0.6233	0.5726
LBα	14.7962	14.7950	1.2162	0.6786	0.6199	0.5682

of grid points. The time-dependent Kohn-Sham equations [Eq. (1)] are solved by means of the second-order split-operator technique in prolate spheroidal coordinates and in the *energy* representation [27,42,43] for the propagation of individual spin orbitals. In this work, we extend this procedure to the numerical solution of the TDDFT calculations for the two-center homonuclear and heteronuclear diatomic molecular systems in the presence of moderate to intense laser fields.

Table I lists the MO energies calculated with the LBα potential, using 70 grid points in the pseudoradial spheroidal coordinate ξ and 30 grid points in the pseudoangular spheroidal coordinate η. The agreement of the calculated valence MO energies with the experimental data is well within 0.01 a.u. Also, since we will be focusing on the excited states for CO and N_2 molecules in Table II, we list the vertical excitation energies for some excited states and compare with experimental data. To calculate the excited states in Table II, we also use the same number of grid points as in Table I. When solving Eq. (1), the pseudoradial coordinate is restricted to the domain from 0 to 40 a.u.; between 20 and 40 a.u. we apply an absorber which smoothly brings down the wave function for each spin orbital without spurious reflections. For the time propagation, we use 4096 time steps per optical cycle (81 920 steps for the whole pulse).

III. BELOW- AND NEAR-THRESHOLD HARMONIC GENERATION: EXCITED-STATE RESONANCE STRUCTURES

After the time-dependent spin orbitals $\psi_{i\sigma}$ are obtained, the induced dipole moment can be expressed as follows:

$$\boldsymbol{d}(t) = \sum_{i\sigma} \langle \psi_{i\sigma}(\boldsymbol{r},t)|\boldsymbol{r}|\psi_{i\sigma}(\boldsymbol{r},t)\rangle. \tag{9}$$

The spectral density of the radiation energy is given by the following expression:

$$S(\omega) = \frac{4\omega^4}{3\pi c^3}\left|\int_{-\infty}^{\infty} \boldsymbol{d}(t)\exp(-i\omega t)dt\right|^2. \tag{10}$$

Here, ω is the frequency of radiation, c is the velocity of light. $S(\omega)$ has the meaning of the energy emitted per unit frequency range at the particular photon frequency ω.

We will focus first on the heteronuclear diatomic molecule carbon monoxide (CO). The HHG spectrum $S(\omega)$ is shown in Fig. 1 for the CO molecule with a range of driving laser intensities $I_0 = (1-8)\times 10^{13}$ W/cm^2 and a wavelength of 730 nm for a 20-optical-cycle sine-squared laser pulse [Eq. (14)]. In Fig. 1, we have clearly identified the excited-state resonance peaks at photon energies 0.3931, 0.4306, and 0.4555 a.u. (all in the VUV region), which correspond to the bound-bound transitions from $5\sigma - 6\sigma$, $5\sigma - 7\sigma$, and $5\sigma - 8\sigma$, respectively. These resonance peaks are similar to the atomic emission lines we recently observed and identified along with experimentalist for Ar atoms [4]. In Figs. 1(a)–1(c) we study the evolution of the resonance peaks as a function of different driving laser intensities. In Fig. 1(a), we only observe the $(5\sigma - 7\sigma)$ resonance peak in this intensity range. This is due to the fact the $5\sigma - 7\sigma$ resonance peak is near (almost embedded) to the nonresonance dipole allowed 7$^{\text{th}}$ order harmonic (H7), and also the 7σ excited state has largest value for the transition

TABLE II. Vertical excitation energies, from the HOMO of the CO (5σ) and N_2 ($3\sigma_g$) molecules, calculated with the LBα potential, and the experimental values (in a.u.).

			CO			
Orbital	$5\sigma - 6\sigma$	$5\sigma - 7\sigma$	$5\sigma - 8\sigma$	$5\sigma - 9\sigma$	$5\sigma - 10\sigma$	$5\sigma - 11\sigma$
Expt. [48]	0.3961	0.4188	0.4547	0.4623		
LBα	0.3836	0.4192	0.4523	0.4624	0.4689	0.4779
			N_2			
Orbital	$3\sigma_g - 2\pi_u$	$3\sigma_g - 3\sigma_u$	$3\sigma_g - 4\sigma_u$	$3\sigma_g - 5\sigma_u$	$3\sigma_g - 6\sigma_u$	$3\sigma_g - 7\sigma_u$
Expt. [48]	0.4745	0.4754	0.5277			
LBα	0.4770	0.4771	0.5273	0.5416	0.5507	0.5536

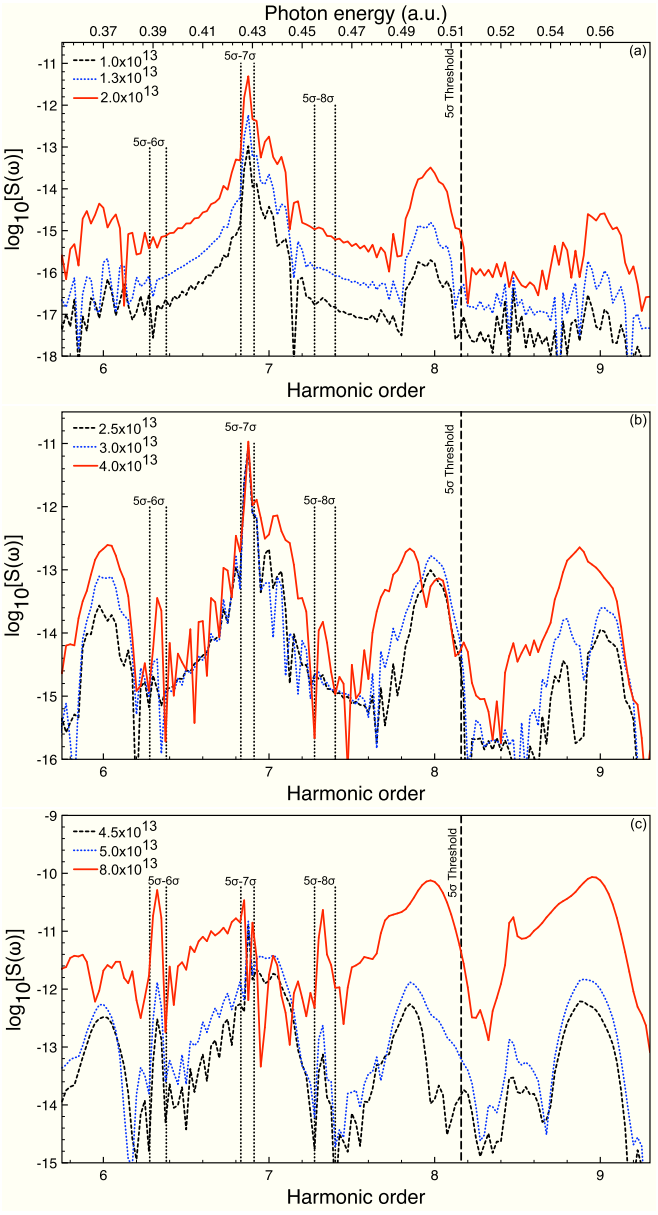

FIG. 1. HHG spectrum $S(\omega)$ of the CO molecule in the $\sin^2$ laser pulse with a peak intensity of (a) $I_0 = (1-2) \times 10^{13}$ W/cm^2, (b) $I_0 = (2.5-4) \times 10^{13}$ W/cm^2, and (c) $I_0 = (4.5-8) \times 10^{13}$ W/cm^2. The laser pulse has a wavelength of 730 nm and a time duration of 20 optical cycles. Each excited-state resonance peak is embedded within two vertical black dotted lines.

dipole (see Table III) of the three excited states studied here. These are also the reasons that the $5\sigma - 7\sigma$ resonance peak is more intense than other resonance peaks [$(5\sigma - 6\sigma)$ and $(5\sigma - 8\sigma)$] in Figs. 1(a)–1(c). Once the driving laser intensity is increased to $I_0 = 2.5 \times 10^{13}$ W/cm^2 we start to observe the $5\sigma - 6\sigma$ resonance peak [Fig. 1(b)]. As the driving laser intensity is further increased to $I_0 = 4 \times 10^{13}$ W/cm^2, the $5\sigma - 8\sigma$ resonance peak appears [Fig. 1(b)]. In Fig. 1(c), all three excited-state resonance peaks are clear and sharp peaks (narrow linewidths) up to a driving laser intensity of $I_0 = 8 \times 10^{13}$ W/cm^2. After increasing the driving laser intensity beyond $I_0 = 8 \times 10^{13}$ W/cm^2 (not shown here), the peaks become shifted and broadened and no resonance peaks can be clearly observed for intensities higher than $I_0 = 1 \times 10^{14}$ W/cm^2.

TABLE III. Excited-state transition dipoles $\langle \Psi_f | z | \Psi_i \rangle$, from the HOMO ($\Psi_i$) of the CO ($5\sigma$) and N_2 ($3\sigma_g$) molecules at $t = 0$ (in a.u.).

	CO		
Excited state (f)	6σ	7σ	8σ
$\lvert\langle \Psi_f \lvert z \rvert \Psi_{5\sigma} \rangle\rvert$	0.2195	0.4084	0.1889
	N_2		
Excited state (f)	$3\sigma_u$	$4\sigma_u$	$5\sigma_u$
$\lvert\langle \Psi_f \lvert z \rvert \Psi_{3\sigma_g} \rangle\rvert$	0.3890	0.1643	0.0194

Now, we will turn our attention to the nitrogen (N_2) homonuclear diatomic molecule. The HHG spectrum $S(\omega)$ is shown in Fig. 2 for the N_2 molecule and has the same range of driving laser intensities, wavelength, and time duration as calculated for the CO molecule in Fig. 1. In Fig. 2, we have also clearly identified the N_2 molecules excited-state resonance peaks at photon energies 0.4805, 0.5304, and 0.5660 a.u. (all in the EUV region), which correspond to the bound-bound transitions from $3\sigma_g - 3\sigma_u$, $3\sigma_g - 4\sigma_u$, and $3\sigma_g - 5\sigma_u$, respectively. In Figs. 2(a)–2(c), we study the evolution of the resonance peaks as a function of different driving laser intensities. The $3\sigma_g - 5\sigma_u$ resonance peak photon energy 0.5660 a.u. is very close to the $3\sigma_g$ ionization threshold (0.5682 a.u.). Also, the $3\sigma_g - 5\sigma_u$ resonance peak is embedded in the 9$^{\text{th}}$ order harmonic (H9) which spans photon energies both above and below the threshold. In Fig. 2(a), we observe all three excited-state ($3\sigma_g - 3\sigma_u$, $3\sigma_g - 4\sigma_u$, and $3\sigma_g - 4\sigma_u$) resonance peaks at lower driving laser intensities [$I_0 = (1-2) \times 10^{13}$ W/cm^2] as compared to the CO molecule in in Fig. 1(a). In Table III, the excited-state transition dipoles for the N_2 molecule are decreasing in value the higher the excited state. This is also the trend we observe in Fig. 2, hence, the resonance peak intensity $S(\omega)$ has the following trend:

$$(3\sigma_g - 5\sigma_u) < (3\sigma_g - 4\sigma_u) < (3\sigma_g - 3\sigma_u). \tag{11}$$

At larger driving laser intensities [$I_0 = (2.5-4) \times 10^{13}$ W/cm^2] in Fig. 2(b) the $3\sigma_u - 5\sigma_u$ resonance peak starts to broaden, and as the driving laser intensity is increased the peak is no longer distinguishable and totally embedded in the 9$^{\text{th}}$ order harmonic at a driving laser intensity of $I_0 = 4 \times 10^{13}$ W/cm^2. The $3\sigma_g - 3\sigma_u$ and $3\sigma_g - 4\sigma_u$ resonance peaks in Fig. 2(b) still exhibit narrow linewidths for these driving laser intensities. In Fig. 2(c), for stronger driving laser intensities we observe the $3\sigma_g - 3\sigma_u$ and $3\sigma_g - 4\sigma_u$ resonance peaks start to broaden for a laser intensity of $I_0 = 8 \times 10^{13}$ W/cm^2 and nearly vanish (very broad) for laser intensities greater than $I_0 = 1 \times 10^{14}$ (not shown here).

Since we use an absorber when solving the time-dependent Kohn-Sham equations (1), the normalization integrals of the spin orbitals decrease in time, thus describing ionization. The ionization probability can be calculated from the normalization of the wave function at the end of the laser pulse:

$$P = 1 - \prod_{i\sigma} N_{i,\sigma}(T), \tag{12}$$

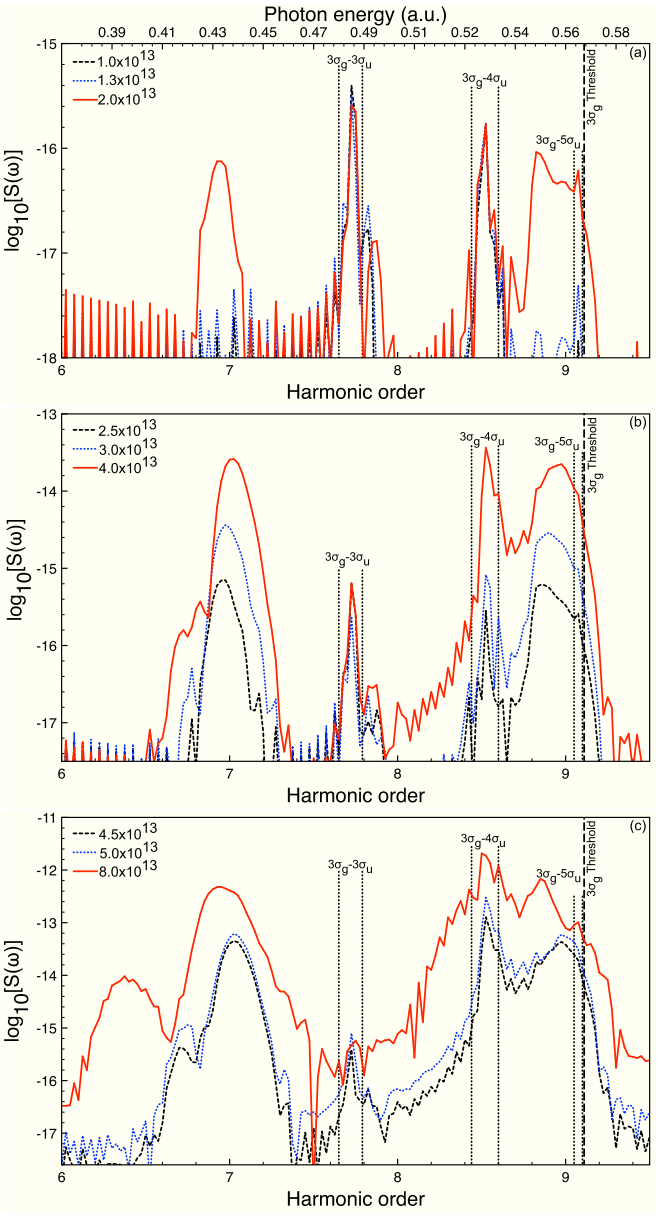

FIG. 2. HHG spectrum $S(\omega)$ of the N_2 molecule in the $\sin^2$ laser pulse with a peak intensity of (a) $I_0 = (1-2)\times 10^{13}$ W/cm^2, (b) $I_0 = (2.5-4)\times 10^{13}$ W/cm^2, and (c) $I_0 = (4.5-8)\times 10^{13}$ W/cm^2. The laser pulse has a wavelength of 730 nm and a time duration of 20 optical cycles. Each excited-state resonance peak is embedded within two vertical black dotted lines.

where

$$N_{i,\sigma}(T) = \langle \psi_{i,\sigma}(T) | \psi_{i,\sigma}(T) \rangle \tag{13}$$

is the normalization (survival probability) of the $i\sigma$th spin orbital after the pulse. In Fig. 3, we show the intensity dependence of the multiphoton total ionization (MPI) probabilities at the end of the sine-squared laser pulse ($t = T$). The degree of nonlinearity $\{d(\log P)/d(\log I_0)$ where P [Eq. (12)] is the total ionization probability$\}$ is close to 5. We note that the intensity range used in the calculations is beyond the applicability of the lowest-order perturbation theory, where the ionization probability P must be proportional to I_0^N, N being

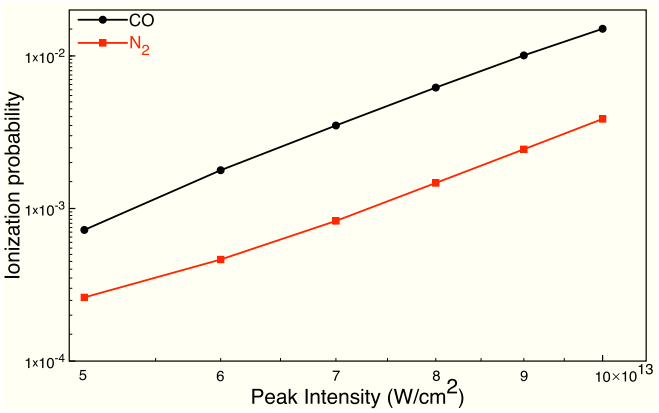

FIG. 3. Ionization probabilities of CO and N_2 molecules versus the peak intensity of the sine-squared [$E_{LS}(t)$] laser pulse.

the minimum number of photons required for ionization (in the case of N_2 and CO molecules subject to 730-nm radiation, $N = 10$). Thus, the calculated nonlinearity degree differs from that predicted by the lowest-order perturbation theory.

IV. FIELD-CONTROLLED RESONANCE ENHANCED STRUCTURES

Hereafter, we will focus on the control and enhancement of the VUV excited-state resonance peaks for the CO molecule and the EUV excited-state resonance peaks for the N_2 molecule. Our main goal is to enhance [increase the intensity of $S(\omega)$] the resonance structures orders of magnitude while still keeping the resonance peaks sharp and narrow. We have chosen to control and enhance the resonance structures by laser field control, hence, with different laser pulse shapes. The NIR laser intensity will be $I_0 = 4\times 10^{13}$ W/cm^2 for the CO molecule and $I_0 = 1.3\times 10^{13}$ W/cm^2 for the N_2 molecule. At these laser intensities, the CO and N_2 molecules excited-state resonance peaks have narrow linewidths, and all three excited states are populated and clearly visible in Fig. 1 for CO and in Fig. 2 for N_2. We will try five different types of laser pulse shapes to control and increase the total ionization probability for the CO and N_2 molecules, therefore enhancing the excited-state resonance structures.

We first consider the NIR sine-squared laser pulse $E_{LS}(t)$ which has the following form:

$$E_{LS}(t) = F_L \sin^2 \frac{\pi t}{T_L} \sin \omega_L t, \tag{14}$$

where $T_L = 2\pi/\omega_L$ and ω_L denote the pulse duration and the carrier frequency [here we choose the laser wavelength as 730 nm ($\omega_L = 0.0624$ a.u.)], respectively; F_L is the NIR peak field strength. The pulse has a duration of 20 optical cycles ($\sim$49 fs) and is shown along with its Fourier transform in Fig. 4. These are the same laser parameters we used in Figs. 1 and 2.

Next, the $E_X(t)$ XUV (XUV will be labeled for the laser pulse, and we will use EUV for the excited-state resonance peaks) laser pulse has the form

$$E_X(t) = F_X \sin^2 \frac{\pi t}{T_X} \sin \omega_X t, \tag{15}$$

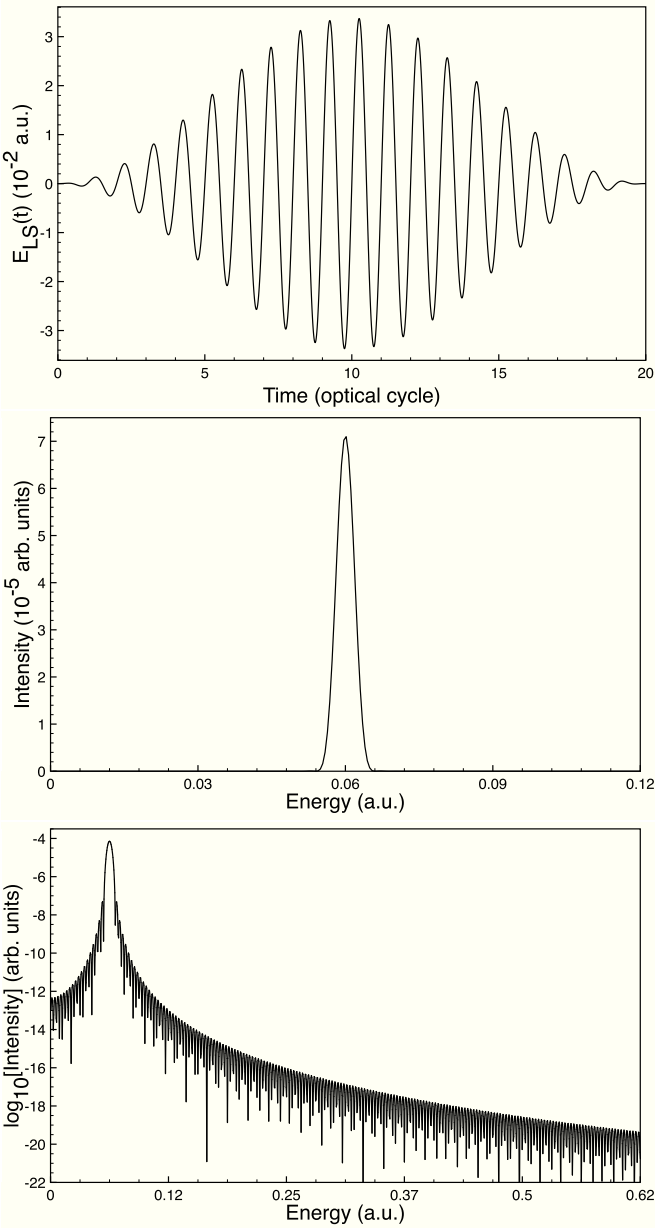

FIG. 4. The NIR sine-squared laser pulse $E_{LS}(t)$ [Eq. (14)] as a function of time (upper panel). The laser has a peak intensity of $I_0 = 4 \times 10^{13}$ W/cm^2 and wavelength 730 nm. The Fourier transform of the $E_{LS}(t)$ laser pulse in linear (middle panel) and log scale (lower panel).

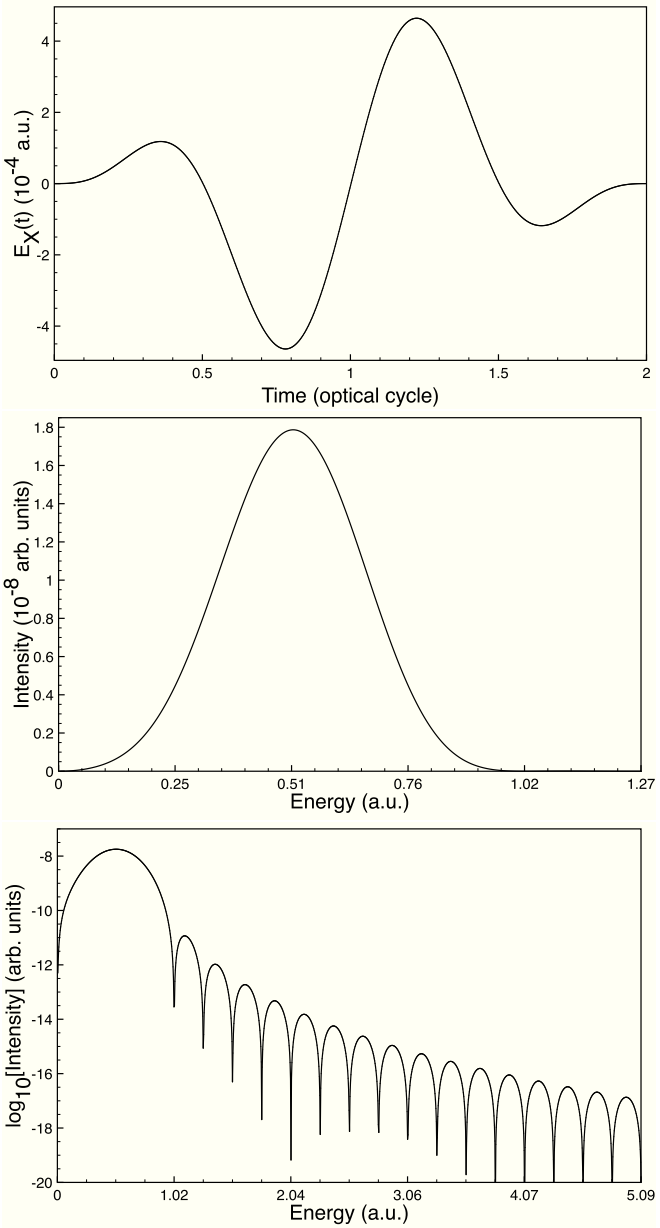

FIG. 5. The XUV sine-squared laser pulse $E_X(t)$ [Eq. (15)] as a function of time (upper panel). The laser has a peak intensity of $I_X = 1 \times 10^{10}$ W/cm^2 and frequency $\omega_X = 0.5093$ a.u. The Fourier transform of the $E_X(t)$ laser pulse in linear (middle panel) and log scale (lower panel).

where $T_X = \frac{2\pi}{\omega_X}$ and ω_X denote the pulse duration and the carrier frequency [here we choose ω_X equal to the HOMO ionization potential for CO ($\omega_X = 0.5093$ a.u.) and N_2 ($\omega_X = 0.5682$ a.u.) molecules]. Here, F_X is the peak field strength of the XUV pulse, and with a pulse duration of two optical cycles (shown in Fig. 5 along with its Fourier transform) (which is ~600 as for the CO molecule and ~535 as for the N_2 molecule). The XUV peak intensity is 1×10^{10} W/cm^2.

The next pulse shape we try is a flat-top NIR laser pulse $E_{LF}(t)$, which has the following form:

$$E_{LF}(t) = 0, \quad 0 \leqslant t < 5T_L \tag{16}$$

$$E_{LF}(t) = F_L \sin \omega_L t, \quad 5T_L \leqslant t \leqslant 15T_L \tag{17}$$

$$E_{LF}(t) = 0, \quad 15T_L < t \leqslant 20T_L \tag{18}$$

where this pulse has a five-optical-cycle field-free propagation at the leading $\{0 \leqslant t < 5T_L$ [Eq. (16)]$\}$ and trailing $\{15T_L < t \leqslant 20T_L$ [Eq. (18)]$\}$ edges and has a flat-top central part of constant peak field strength for 10 optical cycles [Eq. (17)] of the total pulse duration of 20 optical cycles. The flat-top NIR laser pulse is shown along with its Fourier transform in Fig. 6.

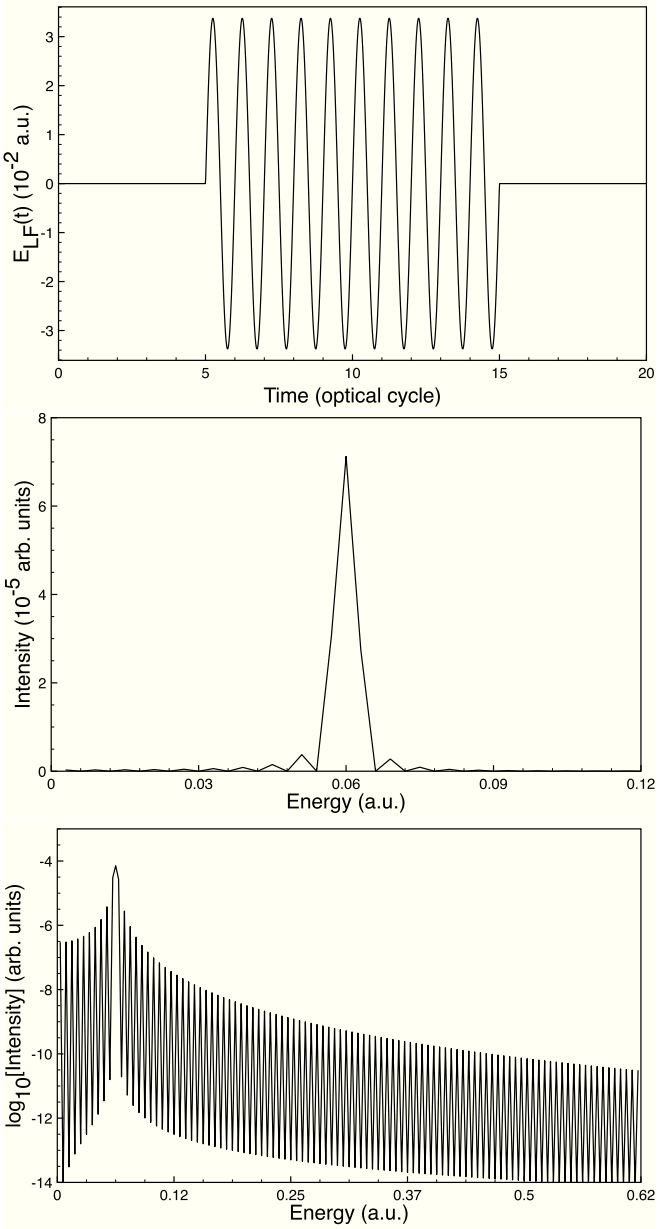

FIG. 6. The flat-top NIR laser pulse $E_{LF}(t)$ [Eqs. (16)–(18)] as a function of time (upper panel). The laser has a peak intensity of $I_0 = 4 \times 10^{13}$ W/cm^2 and wavelength 730 nm. The Fourier transform of the $E_{LF}(t)$ laser pulse in linear (middle panel) and log scale (lower panel).

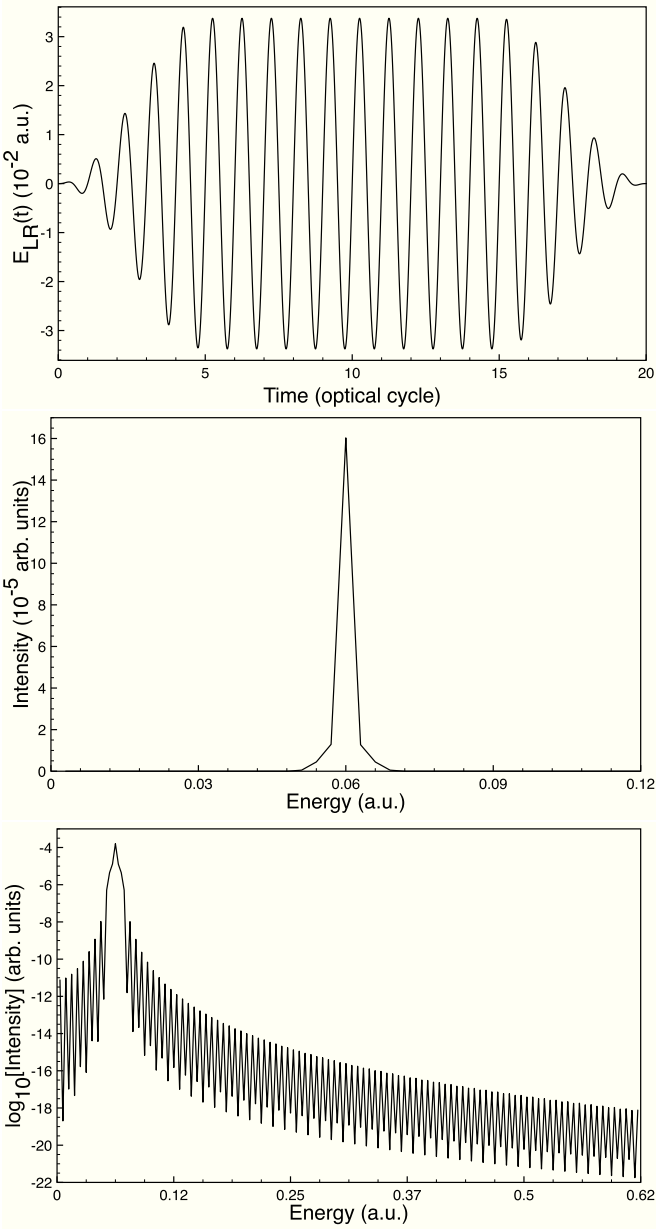

FIG. 7. The sine-squared ramped NIR laser pulse $E_{LR}(t)$ [Eqs. (19)–(21)] as a function of time (upper panel). The laser has a peak intensity of $I_0 = 4 \times 10^{13}$ W/cm^2 and wavelength 730 nm. The Fourier transform of the $E_{LR}(t)$ laser pulse in linear (middle panel) and log scale (lower panel).

Here, the laser parameters (F_L, ω_L, and T_L) are the same as for the $E_{LS}(t)$ laser pulse in Eq. (14).

The last type of pulse we try is a sine-squared ramped NIR laser pulse $E_{LR}(t)$, which has the form

$$E_{LR}(t) = F_L \sin^2 \frac{\pi t}{T_L} \sin \omega_L t, \quad 0 \leqslant t < 5T_L \tag{19}$$

$$E_{LR}(t) = F_L \sin \omega_L t, \quad 5T_L \leqslant t \leqslant 15T_L \tag{20}$$

$$E_{LR}(t) = F_L \sin^2 \frac{\pi t}{T_L} \sin \omega_L t, \quad 15T_L < t \leqslant 20T_L \tag{21}$$

where this pulse has five-optical-cycle sine-squared ramps at the leading $\{0 \leqslant t < 5T_L$ [Eq. (19)]$\}$ and trailing $\{15T_L < t \leqslant 20T_L$ [Eq. (21)]$\}$ edges and has a sine-squared central part of constant peak field strength for 10 optical cycles [Eq. (20)] of the total pulse duration of 20 optical cycles. The sine-squared ramped NIR laser pulse is shown along with its Fourier transform in Fig. 7. Also, for this pulse shape the laser parameters (F_L, ω_L, and T_L) are the same as for the $E_{LS}(t)$ laser pulse in Eq. (14). In Table IV, we provide the values of $E_p = \int E^2(t)dt$ (proportional to the total pulse energies) for different pulse shapes shown in Figs. 4–7. As one can see, the total energies differ by a factor of 2 at most.

TABLE IV. Values of $E_p = \int E^2(t)dt$ for different pulse shapes for the peak intensity 4×10^{13} W/cm^2 and wavelength 730 nm (in a.u.).

Laser pulse $E(t)$	E_p
$E_{LF}(t)$	11.5
$E_{LS}(t)$	8.6
$E_{LR}(t)$	15.8
$E_X(t) + E_{LS}(t)$	8.6

Certainly, this difference cannot explain a several orders of magnitude enhancement of the resonance peaks revealed by our calculations. It is not the total pulse energy but the pulse shape effects that play a major role here. We also note that the different pulses used here have narrow frequency distributions as seen in Figs. 4–7. In this case, the pulse-shape control can be achieved in the time domain rather than in the frequency domain. Discussion of possible experimental techniques is, however, beyond the scope of this paper.

In Fig. 8, we compare the excited-state resonance peaks $[S(\omega)]$ for the CO molecule as a function of laser pulse shapes. The red line (a) is the sine-squared reference pulse in Eq. (14),

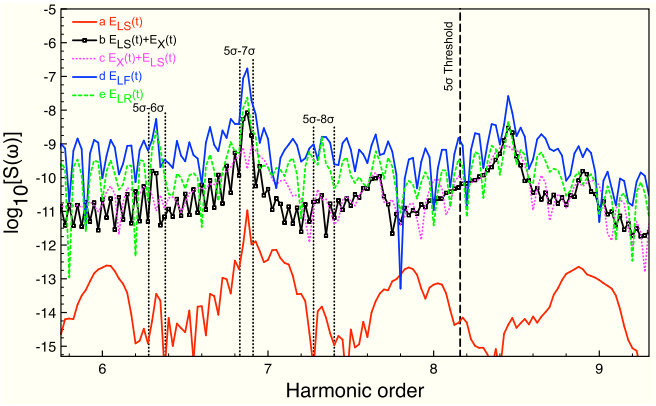

FIG. 8. HHG spectrum $S(\omega)$ of the CO molecule using five different types of laser pulses. All NIR laser pulse shapes (lines a–e) and XUV pulses [lines b (square symbol solid black) and c (dotted magenta)] have a peak intensity of $I_0 = 4 \times 10^{13}$ W/cm^2 and $I_X = 1 \times 10^{10}$ W/cm^2, respectively. Here, for the CO molecule the XUV laser pulse $E_X(t)$ has a carrier frequency of $\omega_X = 0.5093$ a.u. and a pulse duration of ∼600 as (two optical cycles). (a) (Lower solid red line) $E_{LS}(t)$ is the sin^2 NIR laser pulse [Eq. (14)] with a wavelength of 730 nm and a time duration of 20 optical cycles [same laser parameters as in Fig. 1(b)]. (b) The same parameters for the NIR $E_{LS}(t)$ pulse [Eq. (14)] as in (a) with an additional XUV pulse $E_X(t)$ [Eq. (15)] that is turned on at the end [$\sim 19th$ optical cycle of the NIR $E_{LS}(t)$ pulse] of the calculation. (c) The same parameters for the NIR $E_{LS}(t)$ pulse as in (a) with an additional XUV pulse $E_X(t)$ [Eq. (15)] that is turned on at the beginning [$0th$ optical cycle of the NIR $E_{LS}(t)$ pulse] of the calculation. (d) (Upper solid blue line) $E_{LF}(t)$ is the sin^2 NIR flat-top laser pulse [Eqs. (16)–(18)] and (e) (dashed green line) $E_{LR}(t)$ is the ramped sin^2 NIR laser pulse [Eqs. (19)–(21)]. Laser pulses (d) and (e) have the same peak intensity, wavelength, and total time duration as in (a). Each excited-state resonance peak is embedded within two vertical black dotted lines.

which is the pulse shape used in Figs. 1(a)–1(c) to calculate the HHG spectrum for a range of peak intensities. In Fig. 8, all NIR pulse shapes [Fig. 8 (lines a–e)] applied to produce the HHG spectrum use a peak intensity of 4×10^{13} W/cm^2 and the XUV pulse [Fig. 8 (lines b and c)] has a peak intensity of 1×10^{10} W/cm^2. The black line (b) in Fig. 8 makes use of the sine-squared NIR laser pulse in Eq. (14) and a XUV attosecond laser pulse Eq. (15) to give a two-color (NIR+XUV) laser field process. The 600 as XUV laser pulse $[E_X(t)]$ is turned on at the end (48.4 fs) of the 49 fs NIR pulse $[E_{LS}(t)]$. Usually, this type of two-color laser pulse $[E_{LS}(t) + E_X(t)]$ is used for pump-probe measurements where in this process [Fig. 8 (line b)] the NIR pulse would be the pump and the XUV pulse would be the probe. When a CO molecule absorbs a photon from the XUV field with the intensity 1×10^{10} W/cm^2, it can be excited with a substantial probability from the HOMO (5σ) to one of many singly excited states $(5\sigma - n\sigma)$ or to the continuum, depending on the energy of the XUV photon absorbed.

In Fig. 8 (line b), when the NIR pulse comes first, it excites the HOMO (5σ) to the three dominant excited states and at the end of the NIR pulse when the XUV pulse is turned on, it populates more of the HOMO (5σ) to many excited states. When the XUV pulse comes at the very end of the NIR pulse [Fig. 8 (line b)], both pulses can be used as a "pump" pulse. Here, since both the XUV and NIR pulses are used to "pump" the ground state (5σ) to the excited states $(n\sigma)$, we observe an enhancement (∼three orders of magnitude larger) in the resonance peaks in Fig. 8 (line b) compared to the reference sine-squared NIR pulse [Fig. 8 (line a)]. In Fig. 8 (line c), we have the opposite to (line b), now the XUV pulse and the NIR pulse are turned on at the same time. The XUV pulse only has a time duration of 600 as, which is very short compared to the NIR pulse of 49 fs. When the XUV pulse populates the ground state to many excited states and is then turned off, the NIR pulse is strong for these already populated excited states and further one-photon (NIR) transitions can occur or the CO molecule can be ionized. Also, we see splitting of the excited-state resonance peaks into subpeaks in Fig. 8 (line c). It is understood that such additional peaks arise due to excitation of other molecular levels by the combination of the XUV and NIR fields, which, in fact, we recently observed and identified the mechanism for peak splitting in He [49] and Ar [50] atoms in two-color two-photon (XUV+NIR) processes. Here, we have identified when the XUV pulse is turned on at the beginning of the calculation [Fig. 8 (line c)] along with the NIR pulse the excited-state resonance peaks split into subpeaks. Therefore, this two-color laser pulse process in Fig. 8 (line c) can not produce narrow linewidth VUV line emissions for the CO molecule.

Figure 8 (line d) makes use of a flat-top single-color NIR laser pulse given by Eqs. (16)–(18). The flat-top pulse has a central part with a constant peak field strength of 4×10^{13} W/cm^2 for 10 optical cycles of the total 20 optical cycles duration. The flat-top pulse increases the total ionization probability to 5×10^{-5}, as compared to the reference sine-squared pulse [Fig. 8 (line a)] where the total ionization probability is equal to 5×10^{-6}. Since the flat-top laser pulse increases the total ionization probability compared to sine-squared pulse at the same peak field strength (4×10^{13} W/cm^2), the intensity

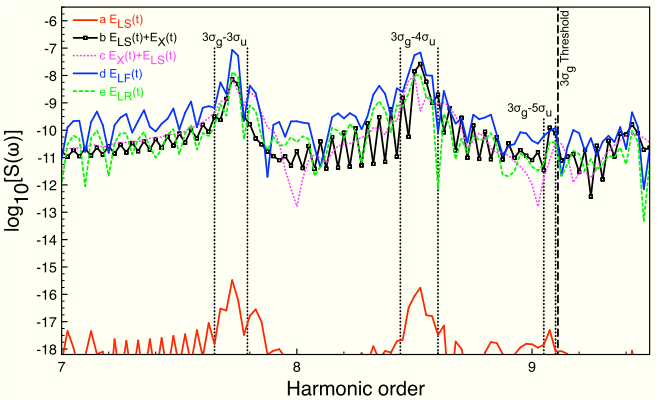

FIG. 9. HHG spectrum $S(\omega)$ of the N_2 molecule using five different types of laser pulses or pulse shapes. All NIR laser pulse shapes (lines a–e) and XUV pulses (lines b and c) have a peak intensity of $I_0 = 1.3 \times 10^{13}$ W/cm^2 and $I_X = 1 \times 10^{10}$ W/cm^2, respectively. Here, for the N_2 molecule the XUV laser pulse $E_X(t)$ has a carrier frequency of $\omega_X = 0.5682$ a.u. and a pulse duration of ∼535 as (2 optical cycles). Lines a–e pulse shapes are the same as in Fig. 8. Each excited-state resonance peak is embedded within two vertical black dotted lines.

of the HHG spectrum $S(\omega)$ should also increase. We see this enhancement [increase in $S(\omega)$] in Fig. 8 (line d) where all resonance structures are increased ∼five orders of magnitude as compared to the reference pulse [Fig. 8 (line a)]. While the $6\sigma - 8\sigma$ excited-state resonance peaks are increased orders of magnitude [Fig. 8 (line b)], they still exhibit VUV emissions with narrow linewidths. Also, we see in Fig. 8 (line d) the flat-top laser pulse has the largest enhancement of the HHG spectrum intensity $S(\omega)$ compared to any of the other pulses or pulse shapes.

In Fig. 8 (line e), we use a sine-squared ramped laser pulse given by Eqs. (19)–(21) which also increases the total ionization probability (2×10^{-5}) compared to the sine-squared laser pulse (5×10^{-6}) since the sine-squared ramped laser pulse has a longer time duration with peak field strength (10 optical cycles) than that of the sine-squared pulse. Again, we observe an increase in total ionization probability, so therefore the HHG spectrum intensity $S(\omega)$ is increased [Fig. 8 (line e)] and both the 6σ and 8σ excited-state resonance peaks are enhanced by the exact order of magnitude as with use of the flat-top pulse [Fig. 8 (line d)]. The 7σ excited-state resonance peak is also enhanced with use of the ramped pulse [Fig. 8 (line e)], but not as much as with the flat-top pulse [Fig. 8 (line d)]. In Fig. 8 (lines a–e), we can clearly see that the flat-top and ramped laser pulses produce a narrow linewidth enhanced resonance VUV radiation for the CO molecules excited states ($6\sigma - 8\sigma$).

In Fig. 9, we compare the excited-state resonance peaks [HHG spectrum $S(\omega)$] for the N_2 molecule as a function of laser pulse shapes as we did for the CO molecule in Fig. 8. All pulse shapes are the same as described previously for the CO molecule in Eqs. (14)–(21). For the N_2 molecule, we chose the NIR peak laser intensity (I_0) to be 1.3×10^{13} W/cm^2 and all other NIR laser parameters (ω_L, T_L, and total pulse duration) are the same as for the CO molecule and given previously throughout Eqs. (14)–(21). Here, the XUV peak laser intensity (I_X) is 1×10^{10} W/cm^2 with a time duration of ∼535 as, and $\omega_X = 0.5682$ a.u. is its central frequency. The details of the different pulses [Fig. 9 (lines a–e)] are described previously when discussing Fig. 8 for the CO molecule.

Now, let us turn to the discussion of the enhanced resonance EUV line structures for the N_2 molecules excited states ($3\sigma_u - 5\sigma_u$). In Fig. 9, all pulses or pulse shapes that we applied enhanced the resonance excited-state peaks at least seven orders of magnitude as compared to the sine-squared reference pulse Fig. 9 (line a). The NIR flat-top laser pulse [Eqs. (16)–(18)] enhances the resonance peaks [Fig. 9 (line d)] more than any other pulses or pulse shapes in Fig. 9 compared to the reference pulse [Fig. 9 (line a)]. By using the NIR flat-top laser pulse [Fig. 9 (line d)], the resonance peaks are enhanced eight orders of magnitude as compared to the reference pulse [Fig. 9 (line a)]. Again, since the flat-top laser pulse increases the total ionization probability (1.3×10^{-5}) as compared to the sine-squared pulse total ionization probability (3.0×10^{-6}), therefore the resonance peaks $S(\omega)$ value will be increased. In descending order of resonance enhancement, the next pulse to enhance the resonance peaks seven orders of magnitude is the NIR sine-squared laser pulse in Eq. (14) and a XUV attosecond laser pulse Eq. (15) used together [Fig. 9 (line b)]. For this two-color laser pulse case in Fig. 9 (line b), the XUV laser pulse is turned on near the end (∼$19th$ optical cycle) of the NIR pulse and the XUV laser field has a total pulse duration of ∼535 as. As we have discussed above for the CO molecule case for this type of two-color laser pulse case, when the XUV pulse comes near the end of the NIR pulse, both pulses (NIR and XUV) are acting as "pump" pulses. Again, meaning for the case here, the N_2 molecules HOMO ($3\sigma_g$) is dominantly populated (pumped) to the excited states ($3\sigma_u - 5\sigma_u$) with the NIR pulse, and then when the XUV pulse is turned on (∼$19th$ optical cycle) it further "pumps" the HOMO ($3\sigma_g$) electron to many singly excited states or to the continuum, depending on the energy of the XUV photon absorbed. Next, in descending order of resonance enhancement is the sine-squared ramped laser pulse given by Eqs. (19)–(21) which also increases the total ionization probability (9.6×10^{-6}) compared to the sine-squared laser pulse (3.0×10^{-6}) and, hence, increases the resonance peaks seven orders of magnitude [Fig. 9 (line e)].

Lastly, we look at Fig. 9 (line c) where the NIR sine-squared laser pulse in Eq. (14) and a XUV attosecond laser pulse in Eq. (15) are used together, where for this case the XUV pulse is switched on at the beginning of the calculation, along with the NIR pulse. As explained above for the CO molecule this case (for the N_2 molecule) starts to cause splitting of the excited-state resonance peaks into subpeaks in Fig. 9 (line c) and a dominant narrow linewidth EUV line emission is not observed for the N_2 molecule. In Fig. 9 (lines a–e), we can clearly see that the flat-top and the (NIR+XUV) pulse [Fig. 9 (line b)] would have advantage in producing a narrow linewidth enhanced EUV radiation through the resonance excitation of the $3\sigma_u - 5\sigma_u$ electronic states in N_2 molecules.

V. CONCLUSION

In this article, we have presented a detailed investigation and analysis of a regime of below- and near-threshold HHG,

characterized by narrow linewidth resonance structures, which can be controlled by the temporal behavior of a few-cycle driving laser field. Here, we demonstrate the enhancement of the VUV line radiation for the CO molecule and the EUV line radiation for the N_2 molecule with different types (NIR and XUV) and shapes of laser pulses. We make use of TDDFT with a correct asymptotic long-range $(-1/r)$ potential to ensure that the individual spin orbitals have the proper ionization potentials. Our analysis of the different laser pulses used in the calculations reveals that the best results for enhancement of the resonance structures are achieved with the flat-top, ramped, and NIR + XUV laser pulses. When using these three types of laser pulses, the VUV line emissions for the CO molecule are increased on average by five orders of magnitude and the EUV line emissions for the N_2 molecule are increased on average by seven orders of magnitude compared with the reference sine-squared pulse. We believe that the proposed *all-electron* TDDFT method for the study of below- and near-threshold resonance structures in the HHG spectra can be applied to other atomic and molecular systems and help to search for the conditions to improve the conversion efficiency in generation of coherent VUV and EUV radiation.

ACKNOWLEDGMENTS

This work is partially supported by the Chemical Sciences, Geosciences, and Biosciences, Division of the Office of Basic Energy Sciences, U. S. Department of Energy. We also are thankful for the partial support of the Ministry of Science and Technology of Taiwan and National Taiwan University (Grants No. 105R891401 and No. 105R8700-2). D.A.T. acknowledges the partial support from Russian Foundation for Basic Research (Grant No. 16-02-00233).

[1] F. Krausz and M. Ivanov, Rev. Mod. Phys. **81**, 163 (2009).
[2] K. Midorikawa, Jpn. J. Appl. Phys. **50**, 090001 (2011).
[3] C. Winterfeldt, C. Spielmann, and G. Gerber, Rev. Mod. Phys. **80**, 117 (2008).
[4] M. Chini, X. Wang, Y. Cheng, H. Wang, Y. Wu, E. Cunningham, P.-C. Li, J. Heslar, D. Telnov, S. Chu *et al.*, Nat. Photonics **8**, 178 (2014).
[5] D. Fabris, T. Witting, W. A. Okell, D. J. Walke, P. Matia-Hernando, J. Henkel, T. R. Barillot, M. Lein, J. P. Marangos, and J. W. G. Tisch, Nat. Photonics **9**, 383 (2015).
[6] J. Rothhardt, M. Krebs, S. Hadrich, S. Demmler, J. Limpert, and A. Tunnermann, New J. Phys. **16**, 033022 (2014).
[7] H. Wang, Y. Xu, S. Ulonska, J. S. Robinson, P. Ranitovic, and R. A. Kaindl, Nat. Commun. **6**, 7459 (2015).
[8] T. Popmintchev, M.-C. Chen, D. Popmintchev, P. Arpin, S. Brown, S. Alisauskas, G. Andriukaitis, T. Balciunas, O. D. Mücke, A. Pugzlys *et al.*, Science **336**, 1287 (2012).
[9] H. Mashiko, M. J. Bell, A. R. Beck, M. J. Abel, P. M. Nagel, C. P. Steiner, J. Robinson, D. M. Neumark, and S. R. Leone, Opt. Express **18**, 25887 (2010).
[10] M. Beutler, M. Ghotbi, and F. Noack, Opt. Lett. **36**, 3726 (2011).
[11] U. Graf, M. Fieß, M. Schultze, R. Kienberger, F. Krausz, and E. Goulielmakis, Opt. Express **16**, 18956 (2008).
[12] F. Reiter, U. Graf, M. Schultze, W. Schweinberger, H. Schröder, N. Karpowicz, A. M. Azzeer, R. Kienberger, F. Krausz, and E. Goulielmakis, Opt. Lett. **35**, 2248 (2010).
[13] K. T. Kim, D. H. Ko, J. Park, V. Tosa, and C. H. Nam, New J. Phys. **12**, 083019 (2010).
[14] E. Constant, D. Garzella, P. Breger, E. Mével, C. Dorrer, C. Le Blanc, F. Salin, and P. Agostini, Phys. Rev. Lett. **82**, 1668 (1999).
[15] F. Lindner, W. Stremme, M. G. Schätzel, F. Grasbon, G. G. Paulus, H. Walther, R. Hartmann, and L. Strüder, Phys. Rev. A **68**, 013814 (2003).
[16] C. M. Heyl, J. Güdde, A. L'Huillier, and U. Höfer, J. Phys. B: At., Mol. Opt. Phys. **45**, 074020 (2012).
[17] C.-T. Chiang, A. Blättermann, M. Huth, J. Kirschner, and W. Widdra, Appl. Phys. Lett. **101**, 071116 (2012).
[18] H. Merdji, M. Kovačev, W. Boutu, P. Salières, F. Vernay, and B. Carré, Phys. Rev. A **74**, 043804 (2006).
[19] A. Vernaleken, J. Weitenberg, T. Sartorius, P. Russbueldt, W. Schneider, S. L. Stebbings, M. F. Kling, P. Hommelhoff, H.-D. Hoffmann, R. Poprawe *et al.*, Opt. Lett. **36**, 3428 (2011).
[20] J. Boullet, Y. Zaouter, J. Limpert, S. Petit, Y. Mairesse, B. Fabre, J. Higuet, E. Mével, E. Constant, and E. Cormier, Opt. Lett. **34**, 1489 (2009).
[21] S. Hädrich, M. Krebs, J. Rothhardt, H. Carstens, S. Demmler, J. Limpert, and A. Tünnermann, Opt. Express **19**, 19374 (2011).
[22] S. Hädrich, J. Rothhardt, M. Krebs, F. Tavella, A. Willner, J. Limpert, and A. Tünnermann, Opt. Express **18**, 20242 (2010).
[23] S. Fuchs, C. Rödel, M. Krebs, S. Hädrich, J. Bierbach, A. E. Paz, S. Kuschel, M. Wünsche, V. Hilbert, U. Zastrau *et al.*, Rev. Sci. Instrum. **84**, 023101 (2013).
[24] W. Kohn and L. J. Sham, Phys. Rev. **140**, A1133 (1965).
[25] X. Chu and Shih-I Chu, Phys. Rev. A **63**, 023411 (2001).
[26] C. A. Ullrich, U. J. Gossmann, and E. K. U. Gross, Phys. Rev. Lett. **74**, 872 (1995).
[27] J. Heslar, J. J. Carrera, D. A. Telnov, and S. I. Chu, Int. J. Quantum Chem. **107**, 3159 (2007).
[28] J. Heslar, D. Telnov, and Shih-I Chu, Phys. Rev. A **83**, 043414 (2011).
[29] D. A. Telnov, J. Heslar, and S. I. Chu, in *Theoretical and Computational Developments in Modern Density Functional Theory*, edited by A. K. Roy (Nova Science, New York, 2012), pp. 357–390.
[30] J. Heslar, D. A. Telnov, and S. I. Chu, in *Concepts and Methods in Modern Theoretical Chemistry: Statistical Mechanics*, Vol. 2, edited by S. Ghosh and P. Chattaraj (CRC Press, Boca Raton, 2013), pp. 37–55.
[31] *Time-Dependent Density Functional Theory*, edited by M. A. L. Marques, C. A. Ullrich, F. Nogueira, A. Rubio, K. Burke, and E. K. U. Gross (Springer, Berlin, 2006).
[32] P. R. T. Schipper, O. V. Gritsenko, S. J. A. van Gisbergen, and E. J. J. Baerends, J. Chem. Phys. **112**, 1344 (2000).
[33] R. G. Parr and W. Yang, *Density-Functional Theory of Atoms and Molecules* (Oxford University Press, Oxford, 1989).
[34] R. M. Dreizler and E. K. U. Gross, *Density Functional Theory, An Approach to the Quantum Many-Body Problem* (Springer, Berlin, 1990).
[35] X. M. Tong and Shih-I Chu, Phys. Rev. A **55**, 3406 (1997).

[36] S. I. Chu, J. Chem. Phys. **123**, 062207 (2005).
[37] R. van Leeuwen and E. J. Baerends, Phys. Rev. A **49**, 2421 (1994).
[38] D. A. Telnov, J. Heslar, and Shih-I Chu, Phys. Rev. A **90**, 063412 (2014).
[39] D. A. Telnov and Shih-I Chu, Phys. Rev. A **76**, 043412 (2007).
[40] D. A. Telnov, K. Nasiri Avanaki, and Shih-I Chu, Phys. Rev. A **90**, 043404 (2014).
[41] K. Nasiri Avanaki, D. A. Telnov, and Shih-I Chu, Phys. Rev. A **90**, 033425 (2014).
[42] D. A. Telnov and Shih-I Chu, Phys. Rev. A **80**, 043412 (2009).
[43] X. M. Tong and Shih-I Chu, Chem. Phys. **217**, 119 (1997).
[44] K. Siegbahn, J. Electron Spectrosc. Relat. Phenom. **5**, 3 (1974).
[45] G. Johansson, J. Hedman, A. Berndtsson, M. Klasson, and R. Nilsson, J. Electron Spectrosc. Relat. Phenom. **2**, 295 (1973).
[46] H. Hamnett, W. Stoll, and C. E. Brion, J. Electron Spectrosc. Relat. Phenom. **8**, 367 (1976).
[47] D. W. Turner, C. Baker, A. D. Baker, and C. R. Brundle, *Molecular Photoelectron Spectroscopy* (Wiley, London, 1970).
[48] K. P. Huber and G. Herzberg, *Molecular Spectra and Molecular Structure. IV. Constants of Diatomic Molecules* (Van Nostrand Reinhold, New York, 1979).
[49] J. Heslar, D. A. Telnov, and Shih-I Chu, Phys. Rev. A **89**, 052517 (2014).
[50] J. Heslar, D. A. Telnov, and Shih-I Chu, Phys. Rev. A **91**, 023420 (2015).